Charting human subcortical maturation with *in vivo* 7 T MRI

S. Miletić[a, 1,*], P.-L. Bazin[a,b,1], S.J.S. Isherwood[a], M. C. Keuken[a], A. Alkemade[a,2], B.U. Forstmann[a,2,*]

[1,2] authors contributed equally

Affiliations
[a] University of Amsterdam, Department of Psychology, Integrative Model-based Cognitive Neuroscience research unit (IMCN), Nieuwe Achtergracht 129B, Amsterdam, The Netherlands
[b] Max Planck Institute for Human Cognitive and Brain Sciences, Departments of Neurophysics and Neurology, Stephanstraße 1A, Leipzig, Germany

[*] Corresponding authors:
Steven Miletić, Nieuwe Achtergracht 129B, 1001NK Amsterdam, The Netherlands, E: s.miletic@uva.nl
Birte U. Forstmann, Nieuwe Achtergracht 129B, 1001NK Amsterdam, The Netherlands, E: buforstmann@gmail.com

Declarations of interest: None.

Abstract
The human subcortex comprises hundreds of unique structures. Subcortical functioning is crucial for behavior, and disrupted subcortical function is observed in common neurodegenerative diseases. Despite their importance, human subcortical structures continue to be difficult to study *in vivo*. Here, we zoom in on 17 prominent subcortical structures, by describing their approximate iron and myelin contents and thickness, and by providing detailed accounts of their age-related changes across the normal adult lifespan. The results provide compelling insights into the highly heterogeneous morphometry and intricate age-related variations of these structures. They also show that the locations of these structures shift across the lifespan, which is of direct relevance for the use of standard magnetic resonance imaging atlases. The results further our understanding of subcortical morphometry and neuroimaging properties, and of normal aging processes which ultimately can improve understanding of neurodegeneration.

Introduction

The human subcortex comprises hundreds of unique structures (Alkemade et al., 2013; Forstmann et al., 2017) which gain interest from a broad range of neuroscientific disciplines (e.g., Gordon, 2020; Lozano et al., 2019; Raznahan et al., 2014; Shepherd, 2013; Tian et al., 2020). Subcortical functioning is crucial for normal behavior including decision making (Ding and Gold, 2013), reward processing (O'Doherty et al., 2004; Schultz et al., 1997), and motor behavior (Mink, 1996). Disruption of subcortical structures is observed in common neurodegenerative diseases including Parkinson's disease (Hirsch et al., 1988). A subset of patients with Parkinson's disease receives deep brain stimulation (DBS), which involves neurosurgical placement of microelectrodes targeting subcortical structures to relieve motor symptoms (Fasano and Lozano, 2015; Limousin et al., 1995). Subcortical structures are also of interest as (potential) DBS targets in other common disorders such as major depression and epilepsy (Lozano et al., 2019). Despite their importance, human subcortical structures continue to be difficult to study *in vivo* due to their small size, their close spatial proximity, as well as their biophysical properties. These factors combined hamper visualization when using magnetic resonance imaging (MRI) (Keuken et al., 2018). As a result, the human subcortex continues to be *terra incognita* (Forstmann et al., 2017).

Due to the challenges in visualizing the human subcortex using *in vivo* methods, a common approach for locating structures in human participants is to use atlases (Devlin and Poldrack, 2007; Evans et al., 2012). Stereotactic atlases based on *post mortem* tissue are often used for planning DBS surgery, whereas MRI atlases which provide probabilistic location estimates for individual structures are conventionally used in cognitive neuroscientific research. Subcortical MRI atlases are growing in numbers (Keuken et al., 2014; Lau et al., 2020; Pauli et al., 2018; Trutti et al., 2021; Ye et al., 2021) due to improvements in MRI resolution and contrasts. However, MRI atlases are often developed using anatomical images obtained from young participants, which can cause biases when such atlases are subsequently used to analyze data from older participants as well as patient populations (Evans et al., 2012; Keuken et al., 2013; Samanez-Larkin and D'Esposito, 2008). An important factor to consider is atrophy, which is reflected in reduced volume of grey matter structures with increasing age (Cherubini et al., 2009; Courchesne et al., 2000; Herting et al., 2018; Lemaitre et al., 2012; Raz, 2004; Raz and Rodrigue, 2006; Walhovd et al., 2005), and more space for the ventricles which results in an increase in their volume (Good et al., 2001; Greenberg et al., 2008; Stafford et al., 1988; Walhovd et al., 2005). Other aging effects include decreased myelination (Raz and Rodrigue, 2006; Shen et al., 2008) and increased iron deposition (Daugherty and Raz, 2013; Hallgren and Sourander, 1958; Raz and Rodrigue, 2006; Ward et al., 2014; Zecca et al., 2004), both of which affect the contrast in MR images. Aging effects in the subcortex are documented predominantly for the larger structures (Aquino et al., 2009; Cherubini et al., 2009; Daugherty and Raz, 2013, 2016; Fjell et al., 2013; Greenberg et al., 2008; Herting et al., 2018; Keuken et al., 2017; Raz et al., 2005; Raz, 2004; Raz and Rodrigue, 2006; Raznahan et al., 2014; Walhovd et al., 2005), and alter the appearance of the subcortex on MRI images. These subtle alterations may affect applications of MRI for neuroimaging, ranging from the precise targeting of DBS to the study of activity of these regions in cognitive neuroscience.

Here, we zoom in on 17 subcortical structures using specialized *in vivo* methods tailored for studying the human subcortex, including data from 105 healthy participants (Alkemade et al., 2020a). We estimate the individual structures thicknesses and describe their estimated iron and myelin

distributions across the adult lifespan. We analyze maturation in these subcortical structures providing measures for atrophy and location, increased iron deposition, and myelin degradation.

Results

105 healthy volunteers were scanned using an ultra-high field 7 Tesla magnetic resonance imaging scanner as part of the openly available Amsterdam ultra-high field adult lifespan database project (AHEAD; Alkemade et al., 2020a). A quantitative, multi-modal MP2RAGE-ME sequence (Caan et al., 2019) with 0.7 mm isotropic resolution was used to simultaneously estimate R1, R2* and QSM in a single scanning sequence. For each individual, 17 subcortical structures were delineated using the Multi-contrast Anatomical Subcortical Structures Parcellation (MASSP) technique (Bazin et al., 2020).

For each participant-structure combination, we obtained 15 measures of interest. First, we estimated descriptive statistics (the median and interquartile range, IQR) of the distributions of the structure's thickness, and R1, R2*, and QSM values. To facilitate the interpretation of age-related changes in R1, R2*, and QSM, we used simplified biophysical models to transform these biophysical properties into iron and myelin concentration approximations (see Methods), which we focus on in the present work. For these iron and myelin estimates, we also obtained the median and IQR. Finally, we determined the location (center of mass in 3 Cartesian coordinates) of each structure, after applying an affine transformation to a group template to account for inter-individual differences in intracranial volume and skull shape, while retaining inter-individual variability in anatomy relative to the skull. The glossary provides an overview of all structures and their abbreviations as used here, and all available measures.

Glossary

Regions of interest

AMG: Amygdala	**RN**: Red nucleus
CL: Claustrum	**STN**: Subthalamic nucleus
fx: Fornix	**STR**: Striatum
GPe: Globus Pallidus Externa	**THA**: Thalamus
GPi: Globus Pallidus Interna	**VTA**: Ventral Tegmental Area
ic: Internal Capsule	**LV**: Lateral ventricle
PAG: Periaqueductal grey	3V: Third ventricle
PPN: Pedunculopontine nucleus	4V: Fourth ventricle

Midline structures were parcellated as a single structure, all other structures (indicated by bold-faced letters) were parcellated separately per hemisphere. Abbreviations in italic-faced letters indicate white matter structures.

Outcome measures

R1: Longitudinal relaxation rate	Iron: Concentration estimated using simplified biophysical models based on R2* and QSM
R2*: Effective transverse relaxation rate	Myelin: Concentration estimated using simplified biophysical models based on R1 and R2*
QSM: Quantified susceptibility mapping	Location: Center of mass in cartesian coordinates after an affine transformation to group space
Thickness: Shortest distance between separate structure boundaries	

For all measures except location, we estimated two statistics to describe the *within-structure* distribution: the median and interquartile range (IQR). Both statistics are robust against outlying voxels, resulting from suboptimal delineations.

The median estimates present the overall value for an individual structure and, the IQR provides a measure of the structure homogeneity and image noise. For thickness specifically, the IQR of thickness depends on both the quality of delineation, which can suffer from image noise, and also on the structure's shape: Regularly shaped structures such as the red nucleus are expected to have lower between-voxel variability in voxels than irregular structures such as the striatum.

Figure 1 presents an overview of the overall (across-participant) distributions of the median (top row) and IQR (bottom row) of the iron, myelin, and thickness estimates. There was a large heterogeneity in the human subcortex in terms of iron, myelin, and thickness. The globus pallidus externa and interna, red nucleus, substantia nigra, and subthalamic nucleus, as described previously (Haacke et al., 2005; Hallgren and Sourander, 1958; Ramos et al., 2014), revealed the highest iron concentrations (both median and IQR). In line with our expectations, low iron concentrations in combination with high myelin concentrations were observed in white matter structures such as the internal capsule and the fornix. The estimated myelin concentrations of the subthalamic nucleus, red nucleus, and ventral tegmental area were relatively high, which is reflected by the poor visibility of these structures on T1-weighted images (Keuken et al., 2018). In comparison, the estimated myelin concentrations of the striatum and amygdala were much lower, in line with their intensities comparable to grey matter observations on T1-weighted images. Finally, the thalamus was identified as the thickest structure under study, followed by the striatum, red nucleus, amygdala, and lateral ventricles.

The within-structure IQR of iron roughly scaled with the median estimates. As such, the within-structure variability of the iron estimates of the globus pallidus external and interna, red nucleus, substantia nigra, and subthalamic nucleus were highest. For the myelin concentrations, the IQR did not consistently scale with the median, for example the internal capsule showed a high median but low IQR, and the fornix had a high IQR compared to an average median. For thickness, higher median thicknesses were accompanied by higher interquartile ranges of thickness, with the notable exception of the red nucleus. The red nucleus showed a regular spherical shape, explaining the low within-structure variability in thickness.

Figure 1. Across-participant distributions of median (top row) and interquartile range (IQR; bottom row) of iron (left), myelin (middle), and thickness (right column) per structure. The center line in each box marks the median, box limits are the across-participant interquartile range, and whiskers are at 1.5 times the interquartile range below and above the box limits. Error bars drawn inside boxes indicate 95% confidence intervals around the median, obtained by bootstrapping with 10,000 iterations. Colors indicate the hemisphere (LH = left hemisphere, RH = right hemisphere, Single = structures that are continuous across the hemispheres). ppm = parts per million, mm = millimeter.

Maturation

We next studied subcortical maturation across the adult lifespan by modelling the age-related changes in each structure and measure. As we had no *a priori* hypothesis on lateralization, we collapsed across hemispheres to reduce the total number of estimated models. Using conventional regression, we fit a set of 32 regression model specifications (with, as predictor variables, linear and/or quadratic effects of age, plus sex and potential interactions between sex and age) for all structures and measures individually. The model specification that showed the most parsimonious trade-off between quality of fit and model complexity (as quantified using the Bayesian information criterion (Schwarz, 1978)) was considered the winning model and used for further analyses. Below, we focus on 9 measures that

were interpreted in terms of biological components (iron and myelin; see Methods) and processes (atrophy), and we omitted the underlying R1, R2*, and QSM values. All our data and results, including the quantitative MRI results, have been made available through an interactive online app, which can be accessed via https://subcortex.eu/app (Figure 2).

Winning models identified either linear or quadratic influences of age, which complicated the interpretation and comparison of model's parameter estimates across structures and measures. To provide a measure that allowed us to compare different winning model specifications, we calculated a total age-related change metric as the sum of the absolute yearly changes between 19 and 75 years old, as predicted by the winning model. These values (illustrated in Figure 3) were estimated using the winning regression model, and thus allowed incorporation of all available data.

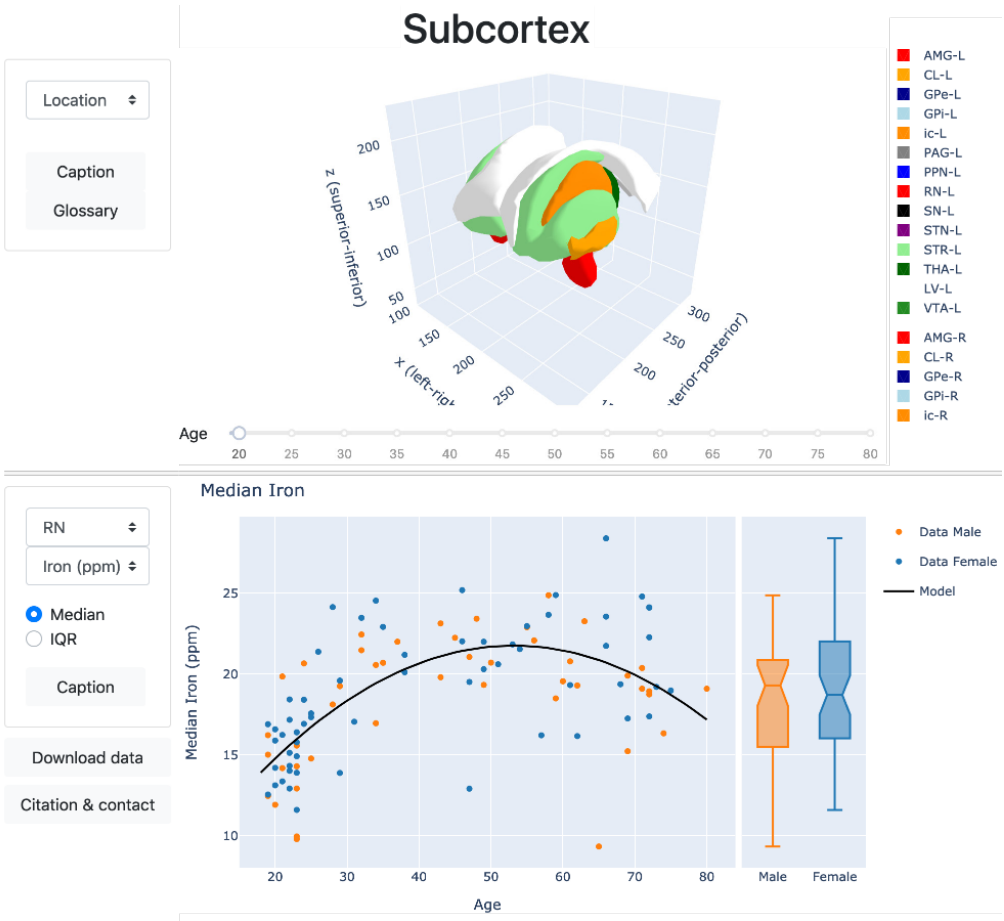

Figure 2. Illustration of the interactive app which allows for visualizing all data and age-related change models. Top panel features a 3D mesh plot that includes all 17 subcortical structures under investigation. The age slider can be used to visualize the age-related changes in center of mass location (currently visible), or the median or interquartile range of iron, myelin, R1, R2*, and QSM values which are color-coded on the individual structures (as selected by the user via a dropdown menu). Bottom panel features scatterplots and boxplots of the relation between age and twelve measures (median and interquartile range of myelin, iron, R1, R2*, QSM, and thickness estimates) for all structures. Optional captions are included, and the data underlying the bottom panel can readily be downloaded as a csv file. The app can be accessed via https://subcortex.eu/app.

As expected, we observed a general iron accumulation across all structures, with the exception of the claustrum and globus pallidus interna (which show stable iron concentrations), and the thalamus (which shows a loss of iron). The other, already iron-rich basal ganglia nuclei continued to accumulate

iron during the adult lifespan, including the red nucleus, substantia nigra, subthalamic nucleus, and globus pallidus externa. We furthermore observed a general myelin degradation, except for the globus pallidus interna and substantia nigra, where no alterations in myelin concentrations were detected. The largest absolute reduction of myelin was present in the fornix.

Based on the IQR measures, we identified a global trend of increasing structure inhomogeneity, which was especially prominent in globus pallidus externa, red nucleus, and striatum. Hence, the (median) iron accumulation and myelin degradation that we noted above for these structures was not evenly spread out within the structure.

Atrophy was reflected in the thinning of individual brain structures and was found to be relatively confined. The fornix, globus pallidus, thalamus, and especially the red nucleus and striatum showed thinning, while the amygdala, claustrum, internal capsule, pedunculopontine nucleus, substantia nigra, subthalamic nucleus, and fourth ventricles did not show any alterations. Ventricular volume increased, which could at least partially be explained by filling of the increasing intracranial space with CSF. This was reflected in thickening of the lateral and third ventricle. We did not observe thickening of the fourth ventricle, potentially due to the specific anatomical characteristics of the cranium. Furthermore, we report thickening of the periaqueductal grey and the ventral tegmental area.

Atrophy of specific subparts of a structure, as a result of increased vulnerability to atrophy in that part, could result in shape changes (Ho et al., 2020; Raznahan et al., 2014). The IQR of thickness is determined partially by the regularity of a structure's shape: Thickness of regularly shaped structures display higher within-structure variability in thickness. Increases in thickness IQR were observed in the amygdala, globus pallidus interna, periaqueductal grey, red nucleus, substantia nigra, thalamus, ventricles and ventral tegmental area. The globus pallidus externa showed a decrease. We would like to point out that the IQR of thickness may also have been affected by (delineation) noise. The increase in thickness IQR could potentially be attributed to reduced visibility of the anatomical structure as a result of altered contrast or increased movement artifacts.

A third potential effect of atrophy is a change in the location of individual structures relative to the skull (Keuken et al., 2017, 2013; Kitajima et al., 2008): As the brain shrinks, the resulting physical space is filled by the CSF, resulting in location shifts for the majority of the brain structures studied. For the majority of structures, with the exception of the ventricles and the ventral tegmental area, the center of mass shifted in the lateral direction with increasing age. The center of mass of the lateral and third ventricles furthermore shifted in the posterior direction, which is potentially indicative of a more pronounced volume increase in the posterior extent of the ventricles. The claustrum, globus pallidus externa, internal capsule, red nucleus, thalamus, fourth ventricle and ventral tegmental area shifted anteriorly. A visual summary of the age-related shifts in structures is available in our online app.

	Iron Median	Myelin Median	Iron IQR	Myelin IQR	Thickness Median	Thickness IQR	Location M-L	Location A-P	Location I-S
AMG	1.47 (0.23)	-0.34 (0.11)	1.13 (0.21)	0.49 (0.10)	0.00 (0.00)	0.18 (0.05)	2.39 (0.19)	0.00 (0.00)	-5.94 (0.57)
CL	0.00 (0.00)	-0.73 (0.30)	0.97 (0.10)	1.18 (1.06)	0.00 (0.00)	0.00 (0.00)	2.18 (0.35)	-2.06 (0.45)	-11.21 (1.78)
fx	0.85 (0.22)	-3.86 (0.72)	1.00 (0.18)	2.61 (2.49)	-0.14 (0.06)	0.00 (0.00)	-	-	-
GPe	2.31 (0.60)	-1.71 (0.31)	3.39 (0.35)	1.67 (0.17)	-0.51 (0.09)	-0.40 (0.08)	6.32 (0.30)	-1.87 (0.34)	-6.77 (0.57)
GPi	0.00 (0.00)	0.00 (0.00)	1.59 (0.59)	1.29 (0.19)	-0.42 (0.07)	0.20 (0.07)	3.03 (0.19)	0.00 (0.00)	-6.38 (0.56)
ic	0.25 (0.06)	-1.54 (0.34)	0.87 (0.12)	0.63 (0.09)	0.00 (0.00)	0.07 (0.02)	3.98 (0.29)	-0.97 (0.15)	-6.66 (0.48)
PAG	0.35 (0.18)	-0.82 (0.18)	0.41 (0.13)	0.26 (0.07)	0.23 (0.04)	0.12 (0.03)	0.58 (0.07)	0.00 (0.00)	-2.87 (0.32)
PPN	0.41 (0.14)	-0.71 (0.13)	0.61 (0.15)	0.11 (0.04)	0.00 (0.00)	0.00 (0.00)	0.93 (0.13)	0.00 (0.00)	-1.82 (0.42)
RN	10.42 (1.38)	-2.21 (0.26)	6.09 (0.70)	1.34 (0.15)	-1.13 (0.21)	0.66 (0.11)	2.04 (0.10)	-1.04 (0.25)	-4.13 (0.48)
SN	3.45 (1.31)	0.00 (0.00)	1.41 (0.30)	0.92 (0.19)	0.00 (0.00)	0.21 (0.05)	2.52 (0.19)	0.00 (0.00)	-3.72 (0.45)
STN	3.83 (0.68)	-1.04 (0.38)	0.66 (0.30)	0.68 (0.17)	0.00 (0.00)	0.00 (0.00)	2.90 (0.33)	0.00 (0.00)	-6.00 (0.59)
STR	3.34 (0.45)	-1.50 (0.26)	6.12 (0.50)	1.62 (0.13)	-1.24 (0.07)	0.25 (0.07)	2.30 (0.21)	0.00 (0.00)	-7.21 (0.45)
THA	-1.40 (1.06)	-0.35 (0.14)	1.75 (0.21)	0.76 (0.15)	-0.40 (0.11)	0.69 (0.12)	3.57 (0.25)	-0.61 (0.15)	-9.22 (0.56)
VTA	1.33 (0.27)	-2.01 (0.60)	1.39 (0.33)	0.00 (0.00)	0.24 (0.05)	0.17 (0.05)	0.00 (0.00)	-0.99 (0.25)	-4.00 (0.47)
LV	-	-	-	-	1.09 (0.28)	0.37 (0.10)	-4.79 (0.47)	9.71 (1.07)	0.00 (0.00)
3V	-	-	-	-	0.75 (0.10)	0.34 (0.09)	0.00 (0.00)	7.67 (0.75)	-7.48 (0.80)
4V	-	-	-	-	0.00 (0.00)	0.00 (0.00)	0.00 (0.00)	-2.51 (0.59)	-5.79 (0.70)

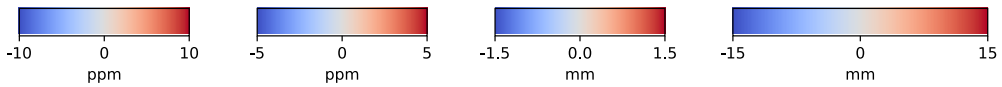

Figure 3. Matrix of cumulative change in all dependent variables (columns) for individual structures (rows). Values indicate the summed absolute change between 19-75 years old. Negative values indicate decreases. Standard errors were obtained by bootstrapping with 10,000 iterations and are shown in parentheses. Location change in fornix was not included since the quality of parcellation of the fornix posterior horns increases with age, resulting in artificial shifts in the estimated center of mass with age. The ventricular system is assumed to have no iron or myelin concentration and is excluded from analysis.

Overall, the maturation effects in subcortical structures were in line with the expected effects on iron accumulation, myelin degradation, and atrophy. Through our studies we now also provide insight into the heterogeneity that is present in the degree to which brain regions are affected.

Between-structure variability in maturation

Next, we aimed to improve understanding of the between-structure similarities and differences in maturation in the median and IQR of iron, myelin, and thickness. To allow comparison of the level of age-related change between the different metrics, we mathematically converted absolute changes of all reported variables to values *proportional* to baseline values, defined as the measure's expected value at 19 years old. In Figure 4, we report these values, split by sex. Relative to baseline values, the red nucleus and striatum showed substantial age-related change, driven by tissue degeneration, iron accumulation, and in the case of the red nucleus a change in the structure's IQR of thickness. Most stable across the lifespan were the ventricles and the pedunculopontine nucleus.

Although for various individual measures we observed sex differences, these were relatively small and confined to specific regions. The most prominent sex differences were in the thickness of the periaqueductal grey, in the pedunculopontine nucleus in which men showed alterations in median iron and myelin IQR, whereas in females only the IQR of iron changed, and in the subthalamic

nucleus females showed a larger change in iron IQR as compared to males. Modest differences were observed in striatum (thickness), amygdala (myelin, thickness), thalamus (myelin, thickness IQR), third ventricle (thickness), internal capsule (iron), claustrum (median myelin), and substantia nigra (iron IQR). Overall, the maturation patterns were comparable across sexes.

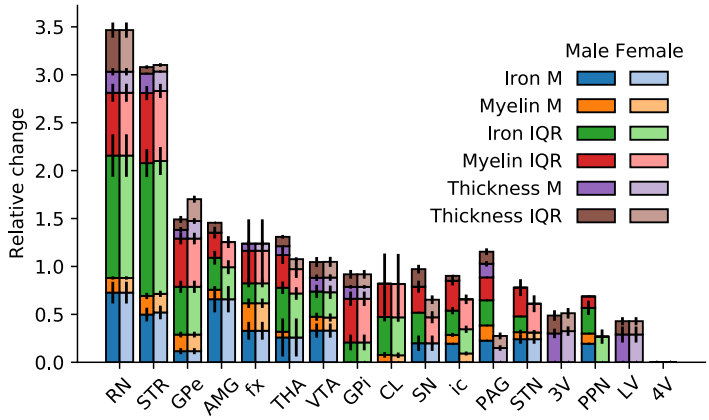

Figure 4. Total (absolute) change per metric between 19 and 75 years, proportional to the metric's value at 19. Error bars indicate standard errors, obtained by bootstrapping with 10,000 iterations.

Figures 3 and 4 indicate that all regions showed maturation, but there was substantial variability between structures in the extent to which they developed and aged. To identify how (dis)similar the regions were, we computed a correlation matrix between all structures, using the matrix visualized in Figure 3 as input (excluding the location changes). The correlation matrix was then organized using a data-driven hierarchical clustering approach, the result of which is shown in Figure 5. The correlation matrix reiterates the presence of a global, across-region maturation process, but includes clusters of regions that covary more strongly together than others. One large cluster shows strong correlations between the maturation patterns of thalamus, striatum, red nucleus, and pedunculopontine nucleus. A second, smaller cluster shows strong correlations between the globus pallidus externa, internal capsule, claustrum, and globus pallidus interna. We also identified regions with maturation patterns that are relatively dissimilar to other regions, such as the fornix, subthalamic nucleus, amygdala, ventral tegmental area, and periaqueductal grey. The ventral tegmental area and periaqueductal grey specifically showed increases in median thickness, which caused negative correlations in their overall maturation patterns since thickness of other regions tended to decrease.

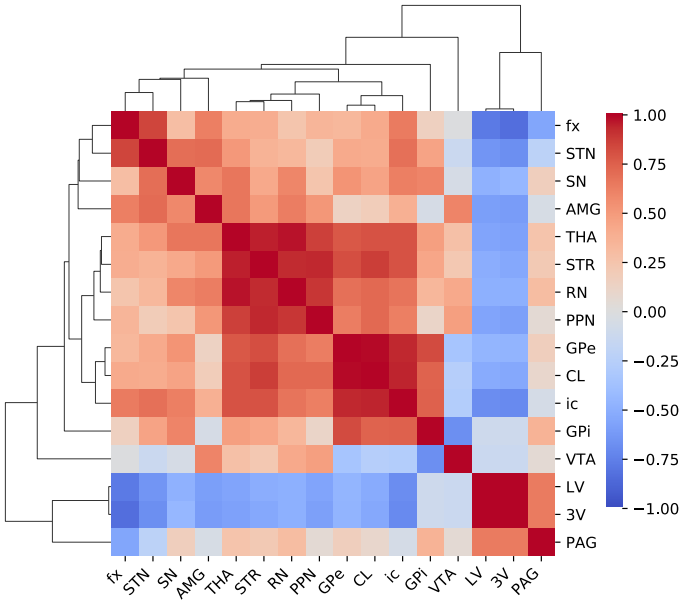

Figure 5. Correlation matrix indicating the similarities and differences between regions' maturation patterns. Regions are ordered using a hierarchical clustering approach, of which the dendrograms are shown on the left and top of the correlation matrix. Colors indicate correlation coefficients. The fourth ventricle is excluded as no age-related changes in this area were found.

Discussion

The human subcortex comprises hundreds of individual structures. Interest in the human subcortex is rapidly growing in cognitive and clinical neuroscience, due to their relevance as (potential) targets for DBS as well as their role in cognition. A detailed understanding of the anatomy and development of the human subcortex is of vital importance for cognitive neuroscience research and the clinical practice. Here, we studied 17 subcortical structures in terms of their iron and myelin content and thickness. Furthermore, we studied the intricate maturation developments in these measures as well as their location.

Our results reveal a heterogeneous image of the human subcortex. Structures vary in their sizes, with the thalamus as the largest, and claustrum the smallest region under study. They furthermore vary in iron content, with the globus pallidus, red nucleus, subthalamic nucleus and substantia nigra being the iron-richest nuclei. In addition to white matter structures, various grey matter nuclei such as the subthalamic nucleus and red nucleus show higher myelination concentrations than cortical grey matter. The maturation patterns in the subcortex are highly heterogenous as well. Overall, our results indicate atrophy, iron accumulation and myelin degradation, and we observed strong variability in aging effects between structures. The red nucleus and striatum show most profound changes, whereas various other structures such as the ventricles and pedunculopontine nucleus remain more stable. Finally, we observe clusters of regions with similar maturation patterns.

We made our results available in an online app which can be used to create interactive and intuitive 3D visualizations of the human subcortex across the lifespan and across modalities. It allows for inspecting and reusing of the underlying models and data of each region individually. The app was designed in a flexible way, so that it can be augmented with more structures and contrasts to expand this comprehensive human subcortex chart. The underlying data can readily be downloaded for further analyses.

Understanding the aging processes in the subcortex is paramount in research and in clinical practice. While iron accumulation is part of normal aging processes, iron dysregulation and increased accumulation in specific subcortical structures such as the striatum are part of multiple neurodegenerative disorders including Parkinson's and Huntington's disease (Andersen et al., 2014; Collingwood and Davidson, 2014; Ward et al., 2014; Zecca et al., 2004). An accurate description of the distributions of iron across the lifespan in health provides a necessary baseline against which pathological iron accumulation can be contrasted, and can serve as a potential biomarker for disease (Guan et al., 2017; Martin et al., 2008; Schenck and Zimmerman, 2004; Zecca et al., 2004). Myelin plays significant roles in plasticity, development and aging in both cortical and subcortical areas (Fields, 2015; Fjell et al., 2013; Grydeland et al., 2019; Hill et al., 2018). Complex patterns of myelin maturation have been proposed to correspond to stages of cognitive development (Turner, 2019). Similar to the case of iron, an understanding of the distributions of myelin in the healthy brain across the lifespan can help identifying and understanding pathological degeneration of myelin in disease (Mancini et al., 2020). As our results show large heterogeneity between regions in iron accumulation and myelin degradation, it is important to understand the age-related changes of each subcortical region individually.

Iron and myelin are the two main determinants of MRI contrast. Many subcortical structures, such as the subthalamic nucleus, cannot readily be distinguished on conventional T1-weighted MRI images due to a lack of contrast with nearby regions. An adequate understanding of the anatomical composition and relative location of the subcortical structures is crucial for planning of MRI scans and of DBS surgery. MRI atlases based on data from young participants or based on post-mortem tissue can lead to biased results when used to analyze participants with a different age (Evans et al., 2012; Samanez-Larkin and D'Esposito, 2008). This is especially relevant in light of our results that show age-related changes in the location of many regions relative to the skull (den Dunnen and Staal, 2005; Keuken et al., 2017, 2013; Kitajima et al., 2008), indicating lateral and inferior shifts across the lifespan. There results should be taken into account when planning of DBS surgery, where stereotactic atlases based on *post mortem* tissue are often used for understanding an individual patient's anatomy. The extent to which the location shifts will furthermore depend on the atrophy present in the individual brain, which could depend on the disease. In cognitive neuroscience research, it is common to apply spatial normalization procedures to a common group space to account for such individual differences in anatomy, but consistent deviations from the group template, such as location shifts due to aging, are likely to lead to normalization errors (Samanez-Larkin and D'Esposito, 2008). Our results can in such cases help understand the biases that could occur when conventional MRI atlases, based on young participants, are used to analyze data from older participants, and call for the development of age-specific MRI atlases of the subcortex to remedy these biases.

The heterogeneity of the subcortex can also provide opportunities to optimize MRI scanning for individual structures. The iron and myelin distributions across structures, as well as the underlying quantitative MRI values, can be used to tailor MR contrasts for visualizing specific structures. The iron-rich nuclei provide clear examples, which are similar in myelin content as neighboring structures and are therefore difficult to visualize in T1-weighed images, but their high iron content leads to strong contrast on QSM and T2*-weighted images. The optimization of MRI protocols extends to the domain of functional neuroimaging. For example, in the case of a T2*-weighted sequence used to estimate blood-oxygen level dependent (BOLD) responses as in a functional experiment, the protocol's echo times could be adjusted to the specific needs for not only the region of interest, but also

the participant's age. Optimized measurement protocols can provide increased contrast-to-noise ratios (de Hollander et al., 2017; Miletić et al., 2020), and thereby improve the sensitivity. Using our online app as a resource for participant-specific predictions of R1, R2*, and QSM values, we envision the use of MRI protocols tailored to the structure of interest and the participant's age and sex. This could be especially useful to improve visualization of small, subcortical structures that are targeted in deep brain stimulation treatments such as the subthalamic nucleus.

Our results extend previous studies into maturation patterns of the subcortex, which focus on a smaller number of typically large subcortical areas, often based on MRI with lower field strengths (Aquino et al., 2009; Cherubini et al., 2009; Daugherty and Raz, 2013, 2016; Fjell et al., 2013; Greenberg et al., 2008; Herting et al., 2018; Keuken et al., 2017; Raz et al., 2005; Raz, 2004; Raz and Rodrigue, 2006; Raznahan et al., 2014; Walhovd et al., 2005). Experiments using very large numbers of participants detected complex nonlinear age-related changes in some subcortical structures (Fjell et al., 2013; Raznahan et al., 2014), suggesting the presence of critical ages that demark changes in the rates of atrophy in some subcortical areas (Fjell et al., 2013). In contrast, we used a cross-sectional sample to estimate more basic maturation models and leveraged the use of ultra-high field 7 T quantitative MRI: Our data allowed for deriving participant-specific masks of 17 unique structures, and for studying a range of different morphometric variables simultaneously. As such, our study provides the most complete description of subcortical morphometry and maturation to date.

Methods

Participants

We made use of the Amsterdam ultra-high field adult lifespan database (AHEAD), which consists of multimodal MRI data from 105 healthy participants. Inclusion criteria were age 18-80 years and self-reported health at the time of inclusion. Exclusion criteria were the absence of a signed informed consent, as well as any factors that could potentially interfere with MRI scanning. This included MRI incompatibility (e.g., pacemakers), pregnancy as well as self-reported claustrophobia. At least six males and females were included in each age decade to ensure full coverage of the adult lifespan. All participants gave written informed consent prior to the onset of data collection. The local ethics board approved the study.

MRI scanning

Images were acquired at the Spinoza Centre for Neuroimaging in Amsterdam, the Netherlands using a Philips Achieva 7T MRI scanner with a 32-channel head array coil. Routine quality checks were performed on a weekly basis at the scanner site. T1w, T2* contrasts were obtained using a MP2RAGEME (multi-echo magnetization-prepared rapid gradient echo) sequence (Caan et al., 2019). The MP2RAGEME is an extension of the MP2RAGE sequence (Marques et al., 2010) and consists of two rapid gradient echo ($GRE_{1,2}$) images that are acquired in sagittal plane after a 180° degrees inversion pulse and excitation pulses with inversion times $TI_{1,2}$ = [670 ms, 3675.4 ms]. A multi-echo readout was added to the second inversion at four echo times (TE_1= 3 ms, $TE_{2,1\text{-}4}$ = 3, 11.5, 19, 28.5 ms). Other scan parameters include flip angles $FA_{1,2}$ = [4°, 4°]; $TR_{GRE1,2}$ = [6.2 ms, 31 ms]; bandwidth = 404.9 MHz; $TR_{MP2RAGE}$ = 6778 ms; acceleration factor SENSE PA = 2; FOV = 205 x 205 x 164 mm; acquired voxel size = 0.70 x 0.7 x 0.7 mm; acquisition matrix was 292 x 290; reconstructed voxel size = 0.64 x 0.64 x 0.7 mm; turbo factor (TFE) = 150 resulting in 176 shots; Total acquisition time = 19.53 min.

Quantitative MRI modeling and parcellation

The MP2RAGEME consists of two interleaved MPRAGEs with different inversions and four echoes in the second inversion. Based on these images, we estimated quantitative MR parameters of R1, R2* and QSM as follows. First, we took advantage of the redundancy in the MP2RAGEME sequence to perform a PCA-based denoising with LCPCA (Bazin et al., 2019). R1 maps were then computed using a look-up table (Marques et al., 2010). R2*-maps were computed by least-squares fitting of the exponential signal decay over the four echoes of the second inversion. Quantitative susceptibility maps were obtained from the phase maps of the second, third, and fourth echoes of the second inversion with TGV-QSM (Langkammer et al., 2015). Skull stripping, required for QSM, was performed on the second inversion, first echo magnitude image (Bazin et al., 2014).

The anatomical regions of interest were defined with the MASSP automated algorithm (Bazin et al., 2020) on the basis of the R1, R2* and QSM image maps. The algorithm combines location, shape, and quantitative MRI priors to define 17 subcortical anatomical regions: striatum (STR), thalamus (THA), lateral, 3rd and 4th ventricles (LV, 3V, 4V), amygdala (AMG), globus pallidus internal segment (GPi) and external segment (GPe), substantia nigra (SN), subthalamic nucleus (STN), red nucleus (RN), ventral tegmental area (VTA), fornix (fx), internal capsule (ic), periaqueductal grey

(PAG), pedunculopontine nucleus (PPN), and claustrum (CL). Separate masks for left and right hemisphere were obtained except for 3V, 4V, and fx.

Iron and myelin approximation

Iron and myelin are main determinants of MR image contrast (Stüber et al., 2014). Several lines of research indicate that the concentration of iron and myelin is approximately linearly related to quantified MRI metrics (qMRI) such as R1, R2* and quantified susceptibility metrics (QSM) (Hametner et al., 2018; Mangeat et al., 2015; Marques et al., 2017; Metere and Möller, 2018; Rooney et al., 2007; Stüber et al., 2014). Assuming a linear relationship between iron and myelin on the one hand, and qMRI on the other, linear models can be fit and used to predict iron and myelin contents based on qMRI values (Metere and Möller, 2018):

$$Iron = Intercept + w_{i,qsm} * QSM + w_{i,R2^*} * R2^* + w_{i.R1} * R1 \quad (1)$$

$$Myelin = Intercept + w_{m,qsm} * QSM + w_{m,R2^*} * R2^* + w_{m,R1} * R1 \quad (2)$$

Estimating the parameters of these models requires (population-average) estimates of iron and myelin content for a variety of regions of interest that cover the range of R1, R2*, and QSM values observed across the brain. Following the approach by Metere and Möller (2018), we obtained these values from the literature (Hallgren and Sourander, 1958; Metere and Möller, 2018 and references therein; Randall, 1938), and supplemented those values using observations in our own *post mortem* tissue (as detailed below). For iron estimates, Hallgren and Sourander (1958) provided quantitative accounts of regions of interest that vary in both iron content and qMRI values and allow stable estimators for the weights in Equation (1). Furthermore, an iron concentration of approximately 0 in the ventricles was assumed, to estimate the intercept of our models.

For myelin estimates, Randall (1938) provides lipid concentrations for the corona radiata, frontal and parietal white matter, brain stem, thalamus, caudate, and frontal and parietal grey matter. Following Metere and Möller (2018), we assumed the lipid concentrations showed linear correlations with myelin concentrations. Unfortunately, these regions do not include iron-rich nuclei, which limits range of (especially) R2* and QSM values with known corresponding lipid concentrations. Using a limited number of regions of interest for a myelin model could limit the generalizability of this model to structures with higher R2* and/or QSM values, such as many basal ganglia structures (e.g. based on only Randall's (Randall, 1938) lipid concentrations, Metere and Möller estimated *negative* myelin concentrations in various basal ganglia structures).

To supplement the literature-based myelin concentrations, we approximated the myelin contents of other regions of interest using a *post mortem* specimen. Here, we made the following assumptions:

1. The optic density of tissue in our silver stains is approximately linearly related to the concentration of myelin in that tissue in our regions of interest (see Figure 6);
2. The myelin concentrations in the *post mortem* specimen are largely representative of the population and comparable to the myelin concentrations reported by Randall (1938);
3. The myelin concentrations in white matter reported by Randall (1938) are comparable to the myelin concentration in the interna capsula. Similarly, the myelin concentrations in parietal cortex are comparable to insular cortex.

Seven 200 μm coronal sections of a single specimen were stained according to the method described by Bielschowsky (for details, see Alkemade et al., 2020b). We confirmed silver stains were

not saturated even in the white matter regions. Sections included the caudate nucleus, thalamus, interna capsula, and insular cortex. We then estimated the median intensity of the lightness of the stain (the optic density) in these four regions. Randall (1938) reports quantified lipid concentrations of the caudate nucleus and thalamus, which can be directly compared to the stain intensities, as well as of parietal grey and white matter. The caudate nucleus, thalamus, and parietal cortex as reported by Randall (1938) were not visible in the same histological section. Caudate nucleus, thalamus, insular cortex and internal capsule where therefore used to provide reference values. For each section separately, we then created a linear calibration curve, which allowed us to determine lipid concentrations based on the stain intensity (Figure 6). Lipid concentrations were then estimated for putamen, globus pallidus, subthalamic nucleus, red nucleus, and substantia nigra.

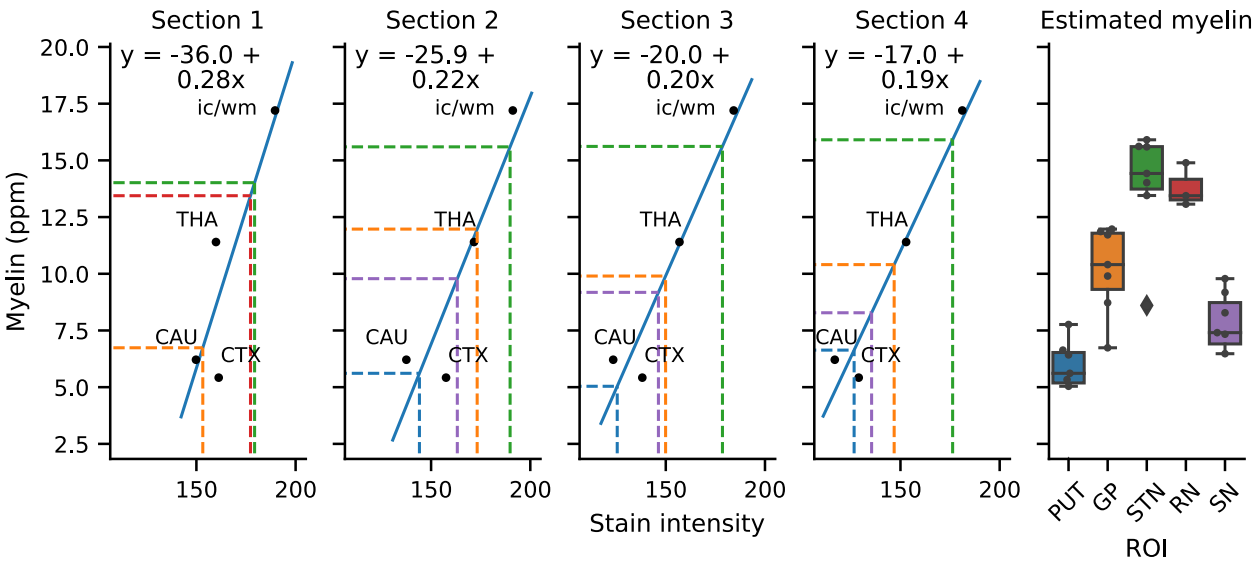

Figure 6. Procedure of estimating myelin contents using a *post mortem* specimen. In each section (seven in total, first four shown), the stain intensities corresponding to CAU, THA, insular cortex (CTX) and the internal capsule (ic/wm) were estimated. For each section individually, a calibration curve was estimated to map stain intensity to myelin values (solid blue lines and equations). Within the range of interest, the relation between stain intensity and myelin content could be approximated with a linear trend. Then, the intensity values for putamen (PUT), GP, STN, RN, and SN were estimated per section (colored dashed lines; note that not all sections contained all structures), and the corresponding myelin values were calculated. Boxplots in the right panel show across-section variability in estimated myelin contents and suggest agreement across sections. The center line in each box marks the median, box limits are the across-section interquartile range, and whiskers are at 1.5 times the interquartile range below and above the box limits. ROI = Region of interest.

qMRI values of the regions for which population-averaged iron and myelin contents were known, were estimated using on the MRI data from AHEAD. Median qMRI values were calculated for these regions using the MASSP masks for subcortical regions, and a MGDM and CRUISE parcellation was used to obtain individual masks for brain stem, cerebellum, and cortex (Bazin et al., 2014). To calculate population-averaged qMRI values, we included only participants of 30 years and older to match the ages of the specimens on which the iron and myelin estimates are based. For brain regions for which we had estimated the myelin content using our *post mortem* specimen (as detailed above), we only included AHEAD subjects of 70 years and older (17 participants total) to approximately match

ages. Tables 1 and 2 list the iron and myelin concentrations, respectively, and their corresponding qMRI values that were used to estimate Equations (1) and (2).

Table 1. Iron estimates and corresponding qMRI values used for estimating linear model Equation (1)
For all regions that were divided in subregions in one but not the other source (i.e. GP vs GPi/GPe; STR vs PUT/CAU; brain stem vs medulla oblongata; and cortical areas), we entered all subregions in the OLS model, using the more specific values where possible, and the global values otherwise. E.g., both GPe and GPi were in the model and shared iron values (Hallgren and Sourander report only GP), but different qMRI values. [a] From Hallgren and Sourander (1958); [b] cerebrospinal fluid estimates from Metere & Moeller (2018); [c] We used the qMRI metrics of the internal capsule here; [d] Cortex, brain stem, cerebellum were parcellated using MGDM and CRUISE (Bazin et al., 2014).

	Iron (ppm)	**QSM (ppm)**	**R1 (Hz)**	**R2* (Hz)**
Brainstem [d]	1.4 [a]	-0.000486	0.808	37.959
CAU	9.28 [a]	0.011508	0.65	47.13
Cerebellum [d]	3.35 [a]	-7.80E-05	0.505	34.069
Frontal Cortex [d]	2.92 [a]	-4.00E-06	0.537	32.722
Frontal White [c]	4.24 [a]	-0.020322	0.895	36.294
GPe	21.3 [a]	0.041336	0.847	83.504
GPi	21.3 [a]	0.044797	0.871	74.822
Motor Cortex [d]	5.03 [a]	-4.00E-06	0.537	32.722
Occipital Cortex [d]	4.55 [a]	-4.00E-06	0.537	32.722
PUT	13.32 [a]	0.011508	0.65	47.13
Parietal Cortex [d]	3.81 [a]	-4.00E-06	0.537	32.722
RN	19.48 [a]	0.05799	0.919	70.737
SN	18.46 [a]	0.053626	0.866	69.493
Sensory Cortex [d]	4.32 [a]	-4.00E-06	0.537	32.722
THA	4.76 [a]	0.00261	0.758	38.272
Temporal Cortex [d]	3.13 [a]	-4.00E-06	0.537	32.722
VENT	0.062 [b]	0.00459	0.343	6.452

Table 2. Myelin estimates and corresponding qMRI values used for estimating linear model Equation (2)
For all regions that were divided in subregions in one but not the other source (i.e. GP vs GPi/GPe; STR vs PUT/CAU; brain stem vs medulla oblongata; and cortical areas), we entered all subregions in the OLS model, using the more specific values where possible, and the global values otherwise. E.g., both CAU and PUT were in the model with separate myelin values, but identical qMRI values since the MASSP parcellation only reports STR. [a] From Randall (1938); [b] cerebrospinal fluid estimates from Metere & Moeller (2018); [c] We used the qMRI metrics of the internal capsule here; [d] Cortex, brain stem, cerebellum were parcellated using CRUISE (Bazin et al., 2014).

	Myelin (ppm)	**QSM (ppm)**	**R1 (Hz)**	**R2* (Hz)**
Brainstem [d]	15.36 [a]	-0.000486	0.808	37.959
CAU	6.21 [a]	0.011508	0.65	47.13
Frontal Cortex [d]	5.08 [a]	-4.00E-06	0.537	32.722
Frontal White [c]	16.26 [a]	-0.020322	0.895	36.294
GPe	10.404 [a]	0.042763	0.815	82.705
GPi	10.404 [a]	0.044215	0.84	71.02

Parietal Cortex [d]	5.42 [a]	-4.00E-06	0.537	32.722
PUT	5.611 [a]	0.011508	0.65	47.13
RN	13.442 [a]	0.05561	0.89	70.264
SN	7.404 [a]	0.047133	0.852	68.453
STN	14.423 [a]	0.045319	0.927	71.019
THA	11.4 [a]	0.00261	0.758	38.272
VENT	0.002 [b]	0.00459	0.232	6.452

To test whether all qMRI metrics were required to predict iron and myelin content, we furthermore fit linear models with all eight possible combinations of R1, R2*, and QSM. Models were fit using ordinary least squares (OLS). For each model, we estimated the Akaike information criterion (AIC; Akaike, 1973) to identify the model that is expected to have the highest predictive performance, and used the model with lowest AIC values (AIC and BIC values agreed on the winning model). We used the AIC here instead of the BIC as the AIC is expected to select models with the highest cross-validated predictive performance, whereas the BIC is expected to select the data-generating model (Wagenmakers and Farrell, 2004). The parametrized winning models were as follows:

$$Iron = -3.6906 + 119.0949 * QSM + 0.2409 * R2^* \quad (3)$$
$$Myelin = -7.7288 + 31.9207 * R1 - 0.1211 * R2^* \quad (4)$$

Figure 7 visualizes quality of fit of the winning models and shows that a high proportion of variance in myelin and iron can be explained using the qMRI values. Note that the model weights cannot directly be compared to the weights from (Stüber et al., 2014), which were obtained using formalin fixated *post mortem* tissue. Formalin fixation can change qMRI values (Birkl et al., 2016; Langkammer et al., 2012; Schmierer et al., 2008; Shepherd et al., 2009; Tovi and Ericsson, 1992). A second complicating factor is that qMRI values can vary between MRI sites (Mancini et al., 2020), suggesting the need to re-estimate model weights when using qMRI obtained at a different site.

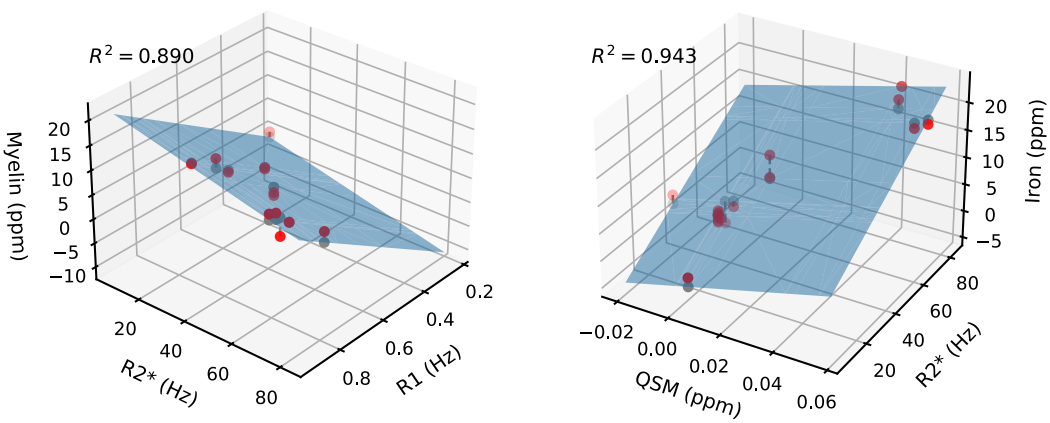

Figure 7. Quality of fit of the myelin (left) and iron (right) model. The planes are given by Equations (3) and (4). Red dots illustrate data points, grey dots are the model predictions for these data points.

Using these simplified biophysical models, we calculated whole-brain iron and myelin maps, and obtained participant-specific myelin and iron values for all structures using the MASSP masks. Iron and myelin maps of a representative participant are shown in Figure 8.

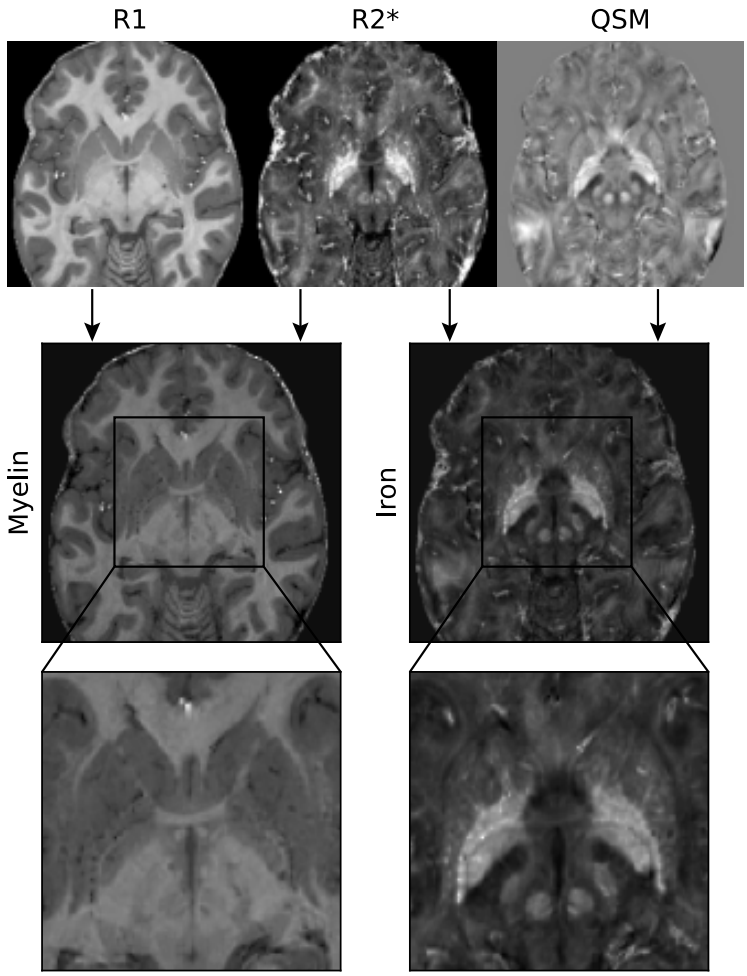

Figure 8. Example of myelin (left) and iron map (right) of a representative participant. The top row shows the R1, R2*, and QSM maps, which were linearly combined into myelin and iron maps (middle and bottom row) using Equations 3-4.

It is important to emphasize that the iron and myelin estimates we report are based on simplifying assumptions with regard to the linearity of the relation between qMRI and iron/myelin, and the iron/myelin concentrations on which the biophysical models are fit (detailed above). As such, the iron and myelin estimates should be not be interpreted as measurements, but rather as approximations that serve to guide the interpretations of qMRI values in terms of the most likely underlying biological contributors to those values.

Thickness estimation

We calculated local structure thickness based on a medial skeleton representation: for each structure, we estimated its skeleton as the ridge equidistant to the structure boundaries. Thickness was defined as twice the distance between the skeleton and the closest boundary, using the method described in Bazin et al. (2020). In other words, local thickness measures at every location inside the structure the distance between the two closest boundaries of that structure, extending the concept of cortical

thickness to more complex shapes. Thickness was chosen here as it, contrary to structure volume, can be determined at the position of each voxel within a structure, thus providing local information. It also appeared more robust than structure volume in our validation experiments. A similar thickness measure was also used in Ho et al. (2020) to detect subtle shape differences.

Center of mass

For all structures, we calculated the center of masses in Cartesian x, y, and z coordinates per participant after an affine transformation to group space, using ANTs (Avants et al., 2008) with mutual information. The affine transformation was applied to correct for inter-individual differences in intracranial volume and skull shape, while retaining inter-individual variability in anatomy relative to the skull.

Age-related change modelling

We describe the age-related changes in iron concentration, myelin content, and thickness, as well as in the center of mass in x, y and z coordinates. For iron, myelin and thickness, we report both a median reflecting the central tendency and interquartile range reflecting structure homogeneity. For thickness, the interquartile range reflects the within-structure variability of thickness, quantifying the regularity of the shape. The MASSP algorithm provided better parcellations of the fornix' horns for the elderly participants compared to the younger participants. As such, the centers of mass of the fornix in the younger participants were biased, and for this reason we did not model age-related change in the center of mass of the fornix.

Exploratory modelling of the between-hemisphere differences per structure suggested no between-hemisphere difference in aging patterns for most structures. Therefore, we subsequently assumed that the age-related changes for each structure were the same in both hemispheres. We collapsed across hemispheres by taking the mean value across both hemispheres per structure and participant to reduce the total number of models estimated.

Per ROI and dependent variable, we fit the following set of 16 potential models: an intercept-only model; a linear effect of age; a quadratic effect of age; a combination of linear and quadratic effects; a combination of linear, quadratic, cubic, and quartic effects; a combination of linear, quadratic, and quartic effects. We furthermore fit the same set of polynomials including an intercept for sex-related differences. Finally, we added a model with main effects of age (linear) and sex combined with an interaction effect, and a model with main effects of age (linear and quadratic) and sex combined with their interaction effects.

Some studies suggest more complex age-related alternations than we estimated, including nonlinear effects (Fjell et al., 2013; Grydeland et al., 2019; Raznahan et al., 2014) and critical ages demarking changes in the rate of atrophy (Fjell et al., 2013) estimated using non-parametric approaches. Such models typically require very large numbers of subjects to obtain robust estimates and are furthermore more difficult to interpret. Therefore, we focus on these relatively parsimonious polynomial models (cf Raznahan et al., 2014), which allows us to determine the general age-related trends in the data.

Models were fit with ordinary least squares (OLS) as implemented in statsmodels (Seabold and Perktold, 2010) for the Python programming language. The quality of fit, penalized with model complexity, was compared using the Bayesian information criterion (BIC; Schwarz, 1978). Lower BIC values indicate more parsimonious trade-offs between quality of fit and model complexity and are preferred. Based on the winning model, we identified influential data points using Cook's distance.

All data points with Cook's distances above 0.20 were further inspected, and removed in case their removal led to a different winning model. The underlying rationale behind this approach is that the winning model should not depend on a limited number of influential observations.

Using the winning age-related change models, we quantified the total age-related changes by summing the yearly absolute changes between 19 and 75 years old (Figure 3). This allows for comparing models with different specifications (e.g., linear vs quadratic models). For winning models that included sex as a predictor (or interactions between sex and age), the cumulative yearly absolute changes were calculated for both sexes and then averaged. For models where the overall direction of the age-related change was negative (identified by comparing the predicted values at 19 and 75 years old), we took the negative of the total age-related changes. Although our data contains a data point of 80 years old, we chose to limit the range of ages that we directly interpret to 19-75 years old, where we expect our models' predictions to be most robust.

For each region, the total age-related changes in median and IQR of iron, myelin, and thickness were divided by their predicted values at 19 years old (Figure 4). As this re-expresses the total change as a proportion of their baseline values, this allows for comparisons between the different measures. We then calculated the correlation matrix to quantify the similarity in age-related changes between regions. The correlation matrix was ordered using a hierarchical clustering with the UPGMA algorithm using the Euclidean distance as a metric (as default settings in the seaborn visualization package (Waskom and Seaborn development team, 2020)), shown in Figure 5.

Confidence intervals and standard errors

Confidence intervals in Figure 1 were obtained using a bootstrapping procedure with 10,000 iterations. We iteratively sampled 105 random observations with replacement from the data, based on which we estimated the median, and then took the 2.5^{th} and 97.5^{th} percentile of the 10,000 medians as the 95% confidence interval. The standard errors in Figures 3 and 4 were obtained using a similar bootstrapping procedure, in which winning model specifications were iteratively fit on 10,000 random samples (all drawn with replacement) from the data. Per iteration, cumulative change metrics were estimated. The standard deviation of the cumulative change metrics across iterations was used to estimate the standard error. For winning models that do not include age as a predictor variable, the standard error is 0 since the cumulative age-related change metric is 0 in each iteration.

Open Science

A prior version of the individual qMRI maps has been released as AHEAD (Alkemade et al., 2020a) can be found at https://doi.org/10.21942/uva.10007840.v1 . All derived participant-wise and region-wise measures can be downloaded from our app at https://subcortex.eu/app . All code used to estimate the models and produce the figures can be found at https://osf.io/mvdbe/ .

Acknowledgements

This research was financially supported by STW/NWO (#14017; BUF and AA), ERC PoC (BUF), NWO Vici (016.Vici.185.052; BUF).

CRediT author statement

Steven Miletić: Conceptualisation, Methodology, Software, Validation, Formal analysis, Investigation, Data curation, Writing – Original draft, Writing – Review & Editing, Visualisation, **Pierre-**

Louis Bazin: Conceptualisation, Methodology, Investigation, Software, Supervision, Writing – Original draft, Writing – Review & Editing, Formal analysis, Data curation, **Scott Isherwood**: Writing – Review & Editing, **Max C. Keuken**: Writing – Review & Editing, **Anneke Alkemade:** Conceptualisation, Methodology, Validation, Investigation, Resources, Data curation, Writing – Original draft, Writing – Review & Editing, Supervision, Project administration, Funding acquisition, **Birte U. Forstmann**: Conceptualisation, Methodology, Validation, Investigation, Resources, Data curation, Writing – Review & Editing, Supervision, Project administration, Funding acquisition.

References

Akaike, H., 1973. Information theory and an extension of the maximum likelihood principle, in: Petrov, B.N., Caski, F. (Eds.), Proceedings of the Second International Symposium on Information Theory. Akademiai Kiado, Budapest, pp. 267–281.

Alkemade, A., Keuken, M.C., Forstmann, B.U., 2013. A perspective on terra incognita: uncovering the neuroanatomy of the human subcortex. Front. Neuroanat. 7, 267–277. https://doi.org/10.3389/fnana.2013.00040

Alkemade, A., Mulder, M.J., Groot, J.M., Isaacs, B.R., van Berendonk, N., Lute, N., Isherwood, S.J., Bazin, P.-L., Forstmann, B.U., 2020a. The Amsterdam Ultra-high field adult lifespan database (AHEAD): A freely available multimodal 7 Tesla submillimeter magnetic resonance imaging database. Neuroimage 221, 117200. https://doi.org/10.1016/j.neuroimage.2020.117200

Alkemade, A., Pine, K., Kirilina, E., Keuken, M.C., Mulder, M.J., Balesar, R., Groot, J.M., Bleys, R.L.A.W., Trampel, R., Weiskopf, N., Herrler, A., Möller, H.E., Bazin, P., Forstmann, B.U., 2020b. 7 Tesla MRI Followed by Histological 3D Reconstructions in Whole-Brain Specimens. Front. Neuroanat. 14, 1–11. https://doi.org/10.3389/fnana.2020.536838

Andersen, H.H., Johnsen, K.B., Moos, T., 2014. Iron deposits in the chronically inflamed central nervous system and contributes to neurodegeneration. Cell. Mol. Life Sci. 71, 1607–1622. https://doi.org/10.1007/s00018-013-1509-8

Aquino, D., Bizzi, A., Grisoli, M., Garavaglia, B., Bruzzone, M.G., Nardocci, N., Savoiardo, M., Chiapparini, L., 2009. Age-related Iron Deposition in the Basal Ganglia: Quantitative analysis in healthy subjects. Radiology 252, 165–172.

Bazin, P.-L., Alkemade, A., Mulder, M.J., Henry, A.G., Forstmann, B.U., 2020. Multi-contrast anatomical subcortical structures parcellation. Elife 9, 1–23. https://doi.org/10.7554/eLife.59430

Bazin, P.-L., Alkemade, A., van der Zwaag, W., Caan, M., Mulder, M., Forstmann, B.U., 2019. Denoising High-Field Multi-Dimensional MRI With Local Complex PCA. Front. Neurosci. 13, 1–10. https://doi.org/10.3389/fnins.2019.01066

Bazin, P.-L., Weiss, M., Dinse, J., Schäfer, A., Trampel, R., Turner, R., 2014. A computational framework for ultra-high resolution cortical segmentation at 7 Tesla. Neuroimage 93, 201–209. https://doi.org/10.1016/j.neuroimage.2013.03.077

Birkl, C., Langkammer, C., Golob-Schwarzl, N., Leoni, M., Haybaeck, J., Goessler, W., Fazekas, F., Ropele, S., 2016. Effects of formalin fixation and temperature on MR relaxation times in the human brain. NMR Biomed. 29, 458–465. https://doi.org/10.1002/nbm.3477

Caan, M.W.A., Bazin, P.-L., Marques, J.P., Hollander, G., Dumoulin, S.O., Zwaag, W., 2019. MP2RAGEME: T1, T2*, and QSM mapping in one sequence at 7 tesla. Hum. Brain Mapp. 40, 1786–1798. https://doi.org/10.1002/hbm.24490

Cherubini, A., Péran, P., Caltagirone, C., Sabatini, U., Spalletta, G., 2009. Aging of subcortical nuclei: Microstructural, mineralization and atrophy modifications measured in vivo using MRI. Neuroimage 48, 29–36. https://doi.org/10.1016/j.neuroimage.2009.06.035

Collingwood, J.F., Davidson, M.R., 2014. The role of iron in neurodegenerative disorders: Insights and opportunities with synchrotron light. Front. Pharmacol. 5 AUG, 1–19. https://doi.org/10.3389/fphar.2014.00191

Courchesne, E., Chisum, H.J., Townsend, J., Cowles, A., Covington, J., Egaas, B., Harwood, M., Hinds, S., Press, G.A., 2000. Normal brain development and aging: Quantitative analysis at in vivo MR imaging in healthy volunteers. Radiology 216, 672–682. https://doi.org/10.1148/radiology.216.3.r00au37672

Daugherty, A., Raz, N., 2013. Age-related differences in iron content of subcortical nuclei observed in vivo: A meta-analysis. Neuroimage 70, 113–121. https://doi.org/10.1016/j.neuroimage.2012.12.040

Daugherty, A.M., Raz, N., 2016. Accumulation of iron in the putamen predicts its shrinkage in healthy older adults: A multi-occasion longitudinal study. Neuroimage 128, 11–20. https://doi.org/10.1016/j.neuroimage.2015.12.045

de Hollander, G., Keuken, M.C., van der Zwaag, W., Forstmann, B.U., Trampel, R., 2017. Comparing functional MRI protocols for small, iron-rich basal ganglia nuclei such as the subthalamic nucleus at 7 T and 3 T. Hum. Brain Mapp. 38, 3226–3248. https://doi.org/10.1002/hbm.23586

den Dunnen, W.F.A., Staal, M.J., 2005. Anatomical alterations of the subthalamic nucleus in relation to age: A postmortem study. Mov. Disord. 20, 893–898. https://doi.org/10.1002/mds.20417
Devlin, J.T., Poldrack, R.A., 2007. In praise of tedious anatomy. Neuroimage 37, 1033–1041. https://doi.org/10.1016/j.neuroimage.2006.09.055
Ding, L., Gold, J.I., 2013. The basal ganglia's contributions to perceptual decision making. Neuron 79, 640–649. https://doi.org/10.1016/j.neuron.2013.07.042
Evans, A.C., Janke, A.L., Collins, D.L., Baillet, S., 2012. Brain templates and atlases. Neuroimage 62, 911–922. https://doi.org/10.1016/j.neuroimage.2012.01.024
Fasano, A., Lozano, A.M., 2015. Deep brain stimulation for movement disorders. Curr. Opin. Neurol. 28, 423–436. https://doi.org/10.1097/WCO.0000000000000226
Fields, R.D., 2015. A new mechanism of nervous system plasticity: Activity-dependent myelination. Nat. Rev. Neurosci. 16, 756–767. https://doi.org/10.1038/nrn4023
Fjell, A.M., Westlye, L.T., Grydeland, H., Amlien, I., Espeseth, T., Reinvang, I., Raz, N., Holland, D., Dale, A.M., Walhovd, K.B., 2013. Critical ages in the life course of the adult brain: Nonlinear subcortical aging. Neurobiol. Aging 34, 2239–2247. https://doi.org/10.1016/j.neurobiolaging.2013.04.006
Forstmann, B.U., de Hollander, G., Van Maanen, L., Alkemade, A., Keuken, M.C., 2017. Towards a mechanistic understanding of the human subcortex. Nat. Rev. Neurosci. 18, 57–65.
Good, C.D., Johnsrude, I.S., Ashburner, J., Henson, R.N.A., Friston, K.J., Frackowiak, R.S.J., 2001. A voxel-based morphometric study of ageing in 465 normal adult human brains. Neuroimage 14, 21–36. https://doi.org/10.1006/nimg.2001.0786
Gordon, E.M., 2020. Functional boundaries within human subcortex. Nat. Neurosci. 23, 1312–1314. https://doi.org/10.1038/s41593-020-00721-4
Greenberg, D.L., Messer, D.F., Payne, M.E., MacFall, J.R., Provenzale, J.M., Steffens, D.C., Krishnan, R.R., 2008. Aging, gender, and the elderly adult brain: An examination of analytical strategies. Neurobiol. Aging 29, 290–302. https://doi.org/10.1016/j.neurobiolaging.2006.09.016
Grydeland, H., Vértes, P.E., Váša, F., Romero-Garcia, R., Whitaker, K., Alexander-Bloch, A.F., Bjørnerud, A., Patel, A.X., Sederevičius, D., Tamnes, C.K., Westlye, L.T., White, S.R., Walhovd, K.B., Fjell, A.M., Bullmore, E.T., 2019. Waves of maturation and senescence in micro-structural MRI markers of human cortical myelination over the lifespan. Cereb. Cortex 29, 1369–1381. https://doi.org/10.1093/cercor/bhy330
Guan, X., Xu, X., Zhang, M., 2017. Region-Specific Iron Measured by MRI as a Biomarker for Parkinson's Disease. Neurosci. Bull. 33, 561–567. https://doi.org/10.1007/s12264-017-0138-x
Haacke, E.M., Cheng, N.Y.C., House, M.J., Liu, Q., Neelavalli, J., Ogg, R.J., Khan, A., Ayaz, M., Kirsch, W., Obenaus, A., 2005. Imaging iron stores in the brain using magnetic resonance imaging. Magn. Reson. Imaging 23, 1–25. https://doi.org/10.1016/j.mri.2004.10.001
Hallgren, B., Sourander, P., 1958. the Effect of Age on the Non-Haemin Iron in the Human Brain. J. Neurochem. 3, 41–51. https://doi.org/10.1111/j.1471-4159.1958.tb12607.x
Hametner, S., Endmayr, V., Deistung, A., Palmrich, P., Prihoda, M., Haimburger, E., Menard, C., Feng, X., Haider, T., Leisser, M., Köck, U., Kaider, A., Höftberger, R., Robinson, S., Reichenbach, J.R., Lassmann, H., Traxler, H., Trattnig, S., Grabner, G., 2018. The influence of brain iron and myelin on magnetic susceptibility and effective transverse relaxation - A biochemical and histological validation study. Neuroimage 179, 117–133. https://doi.org/10.1016/j.neuroimage.2018.06.007
Herting, M.M., Johnson, C., Mills, K.L., Vijayakumar, N., Dennison, M., Liu, C., Goddings, A.L., Dahl, R.E., Sowell, E.R., Whittle, S., Allen, N.B., Tamnes, C.K., 2018. Development of subcortical volumes across adolescence in males and females: A multisample study of longitudinal changes. Neuroimage 172, 194–205. https://doi.org/10.1016/j.neuroimage.2018.01.020
Hill, R.A., Li, A.M., Grutzendler, J., 2018. Lifelong cortical myelin plasticity and age-related degeneration in the live mammalian brain. Nat. Neurosci. 21, 683–695. https://doi.org/10.1038/s41593-018-0120-6
Hirsch, E.C., Graybiel, A.M., Agid, Y., 1988. Melanized dopaminergic neurons are differentially affected in Parkinson's disease. Nature 334, 345--348.
Ho, T.C., Gutman, B., Pozzi, E., Grabe, H.J., Hosten, N., Wittfeld, K., Völzke, H., Baune, B., Dannlowski, U., Förster, K., Grotegerd, D., Redlich, R., Jansen, A., Kircher, T., Krug, A., Meinert, S., Nenadic, I., Opel, N., Dinga, R., Veltman, D.J., Schnell, K., Veer, I., Walter, H., Gotlib, I.H., Sacchet, M.D., Aleman, A., Groenewold, N.A., Stein, D.J., Li, M., Walter, M., Ching, C.R.K., Jahanshad, N., Ragothaman, A., Isaev, D., Zavaliangos-Petropulu, A., Thompson, P.M., Sämann, P.G., Schmaal, L., 2020. Subcortical shape alterations in major depressive disorder: Findings from the ENIGMA major depressive disorder working group. Hum. Brain Mapp. 1–11. https://doi.org/10.1002/hbm.24988
Keuken, M.C., Bazin, P., Backhouse, K., Beekhuizen, S., Himmer, L., Kandola, A., Lafeber, J.J., Prochazkova, L., Trutti, A., Schäfer, A., Turner, R., Forstmann, B.U., 2017. Effects of aging on T1 , T2∗ , and QSM MRI values in the subcortex. Brain Struct. Funct. 222, 2487–2505. https://doi.org/10.1007/s00429-016-1352-4
Keuken, M.C., Bazin, P., Crown, L., Hootsmans, J., Laufer, A., Müller-Axt, C., Sier, R., van der Putten, E.J., Schäfer,

A., Turner, R., Forstmann, B.U., 2014. Quantifying inter-individual anatomical variability in the subcortex using 7T structural MRI. Neuroimage 94, 40–46. https://doi.org/10.1016/j.neuroimage.2014.03.032
Keuken, M.C., Bazin, P.L., Schäfer, A., Neumann, J., Turner, R., Forstmann, B.U., 2013. Ultra-high 7T MRI of structural age-related changes of the subthalamic nucleus. J. Neurosci. 33, 4896–4900. https://doi.org/10.1523/JNEUROSCI.3241-12.2013
Keuken, M.C., Isaacs, B.R., Trampel, R., van der Zwaag, W., Forstmann, B.U., 2018. Visualizing the Human Subcortex Using Ultra-high Field Magnetic Resonance Imaging. Brain Topogr. 31, 513–545. https://doi.org/10.1007/s10548-018-0638-7
Kitajima, M., Korogi, Y., Kakeda, S., Moriya, J., Ohnari, N., Sato, T., Hayashida, Y., Hirai, T., Okuda, T., Yamashita, Y., 2008. Human subthalamic nucleus: Evaluation with high-resolution MR imaging at 3.0 T. Neuroradiology 50, 675–681. https://doi.org/10.1007/s00234-008-0388-4
Langkammer, C., Bredies, K., Poser, B.A., Barth, M., Reishofer, G., Fan, A.P., Bilgic, B., Fazekas, F., Mainero, C., Ropele, S., 2015. Fast quantitative susceptibility mapping using 3D EPI and total generalized variation. Neuroimage 111, 622–630. https://doi.org/10.1016/j.neuroimage.2015.02.041
Langkammer, C., Schweser, F., Krebs, N., Deistung, A., Goessler, W., Scheurer, E., Sommer, K., Reishofer, G., Yen, K., Fazekas, F., Ropele, S., Reichenbach, J.R., 2012. Quantitative susceptibility mapping (QSM) as a means to measure brain iron? A post mortem validation study. Neuroimage 62, 1593–1599. https://doi.org/10.1016/j.neuroimage.2012.05.049
Lau, J.C., Xiao, Y., Haast, R.A.M., Gilmore, G., Uludağ, K., MacDougall, K.W., Menon, R.S., Parrent, A.G., Peters, T.M., Khan, A.R., 2020. Direct visualization and characterization of the human zona incerta and surrounding structures. Hum. Brain Mapp. 41, 4500–4517. https://doi.org/10.1002/hbm.25137
Lemaitre, H., Goldman, A.L., Sambataro, F., Verchinski, B.A., Meyer-Lindenberg, A., Weinberger, D.R., Mattay, V.S., 2012. Normal age-related brain morphometric changes: Nonuniformity across cortical thickness, surface area and gray matter volume? Neurobiol. Aging 33, 617.e1-617.e9. https://doi.org/10.1016/j.neurobiolaging.2010.07.013
Limousin, P., Pollak, P., Benazzouz, A., Hoffmann, D., Le Bas, J.-F., Perret, J.E., Benabid, A.-L., Broussolle, E., 1995. Effect on parkinsonian signs and symptoms of bilateral subthalamic nucleus stimulation. Lancet 345, 91–95. https://doi.org/10.1016/S0140-6736(95)90062-4
Lozano, A.M., Lipsman, N., Bergman, H., Brown, P., Chabardes, S., Chang, J.W., Matthews, K., McIntyre, C.C., Schlaepfer, T.E., Schulder, M., Temel, Y., Volkmann, J., Krauss, J.K., 2019. Deep brain stimulation: current challenges and future directions. Nat. Rev. Neurol. 15, 148–160. https://doi.org/10.1038/s41582-018-0128-2
Mancini, M., Karakuzu, A., Cohen-Adad, J., Cercignani, M., Nichols, T.E., Stikov, N., 2020. An interactive meta-analysis of MRI biomarkers of Myelin. Elife 9, 1–23. https://doi.org/10.7554/eLife.61523
Mangeat, G., Govindarajan, S.T., Mainero, C., Cohen-Adad, J., 2015. Multivariate combination of magnetization transfer, T2* and B0 orientation to study the myelo-architecture of the in vivo human cortex. Neuroimage 119, 89–102. https://doi.org/10.1016/j.neuroimage.2015.06.033
Marques, J.P., Khabipova, D., Gruetter, R., 2017. Studying cyto and myeloarchitecture of the human cortex at ultra-high field with quantitative imaging: R1, R2* and magnetic susceptibility. Neuroimage 147, 152–163. https://doi.org/10.1016/j.neuroimage.2016.12.009
Marques, J.P., Kober, T., Krueger, G., van der Zwaag, W., Van de Moortele, P.F., Gruetter, R., 2010. MP2RAGE, a self bias-field corrected sequence for improved segmentation and T1-mapping at high field. Neuroimage 49, 1271–1281. https://doi.org/10.1016/j.neuroimage.2009.10.002
Martin, W.R.W., Wieler, M., Gee, M., 2008. Midbrain iron content in early Parkinson disease: A potential biomarker of disease status. Neurology 70, 1411–1417. https://doi.org/10.1212/01.wnl.0000286384.31050.b5
Metere, R., Möller, H.E., 2018. Quantifying the myelin and iron contents of the brain in vivo using a linear model of relaxation. Proc. Int. Soc. Magn. Reson. Med. 26.
Miletić, S., Bazin, P.-L., Weiskopf, N., van der Zwaag, W., Forstmann, B.U., Trampel, R., 2020. fMRI protocol optimization for simultaneously studying small subcortical and cortical areas at 7 T. Neuroimage 219. https://doi.org/10.1016/j.neuroimage.2020.116992
Mink, J.W., 1996. The Basal Ganglia: Focused selection and inhibition of competing motor programs. Prog. Neurobiol. 50, 381–425. https://doi.org/10.1016/S0301-0082(96)00042-1
O'Doherty, J., Dayan, P., Schultz, J., Deichmann, R., Friston, K.J., Dolan, R.J., 2004. Dissociable Roles of Ventral and Dorsal Striatum in Instrumental Conditioning. Science (80-.). 304, 452–454. https://doi.org/10.1126/science.1094285
Pauli, W.M., Nili, A.N., Tyszka, J.M., 2018. A high-resolution probabilistic in vivo atlas of human subcortical brain nuclei. Sci. Data 5, 180063. https://doi.org/10.1038/sdata.2018.63
Ramos, P., Santos, A., Pinto, N.R., Mendes, R., Magalhães, T., Almeida, A., 2014. Iron levels in the human brain: A post-mortem study of anatomical region differences and age-related changes. J. Trace Elem. Med. Biol. 28, 13–17. https://doi.org/10.1016/j.jtemb.2013.08.001
Randall, L.O., 1938. Chemical Topography of the Brain. J. Biol. Chem. 124, 481–488.
Raz, N., 2004. The Aging Brain Observed in Vivo, in: Cognitive Neuroscience of Aging. Oxford University Press, pp.

19–57. https://doi.org/10.1093/acprof:oso/9780195156744.003.0002
Raz, N., Lindenberger, U., Rodrigue, K.M., Kennedy, K.M., Head, D., Williamson, A., Dahle, C., Gerstorf, D., Acker, J.D., 2005. Regional brain changes in aging healthy adults: General trends, individual differences and modifiers. Cereb. Cortex 15, 1676–1689. https://doi.org/10.1093/cercor/bhi044
Raz, N., Rodrigue, K.M., 2006. Differential aging of the brain: Patterns, cognitive correlates and modifiers. Neurosci. Biobehav. Rev. 30, 730–748. https://doi.org/10.1016/j.neubiorev.2006.07.001
Raznahan, A., Shaw, P.W., Lerch, J.P., Clasen, L.S., Greenstein, D., Berman, R., Pipitone, J., Chakravarty, M.M., Giedd, J.N., 2014. Longitudinal four-dimensional mapping of subcortical anatomy in human development. Proc. Natl. Acad. Sci. 111, 1592–1597. https://doi.org/10.1073/pnas.1316911111
Rooney, W.D., Johnson, G., Li, X., Cohen, E.R., Kim, S.-G., Ugurbil, K., Springer, C.S., 2007. Magnetic field and tissue dependencies of human brain longitudinal 1H2O relaxation in vivo. Magn. Reson. Med. 57, 308–318. https://doi.org/10.1002/mrm.21122
Samanez-Larkin, G.R., D'Esposito, M., 2008. Group comparisons: Imaging the aging brain. Soc. Cogn. Affect. Neurosci. 3, 290–297. https://doi.org/10.1093/scan/nsn029
Schenck, J.F., Zimmerman, E.A., 2004. High-field magnetic resonance imaging of brain iron: Birth of a biomarker? NMR Biomed. 17, 433–445. https://doi.org/10.1002/nbm.922
Schmierer, K., Wheeler-Kingshott, C.A.M., Tozer, D.J., Boulby, P.A., Parkes, H.G., Yousry, T.A., Scaravilli, F., Barker, G.J., Tofts, P.S., Miller, D.H., 2008. Quantitative magnetic resonance of postmortem multiple sclerosis brain before and after fixation. Magn. Reson. Med. 59, 268–277. https://doi.org/10.1002/mrm.21487
Schultz, W., Dayan, P., Montague, P.R., 1997. A neural substrate of prediction and reward. Science (80-.). 275, 1593–1599. https://doi.org/10.1126/science.275.5306.1593
Schwarz, G., 1978. Estimating the dimension of a model. Ann. Stat. 6, 461–464. https://doi.org/10.1214/aos/1176344136
Seabold, S., Perktold, J., 2010. Statsmodels: econometric and statistical modeling with Python. 9th Python Sci. Conf. 57–61.
Shen, S., Sandoval, J., Swiss, V.A., Li, J., Dupree, J., Franklin, R.J.M., Casaccia-Bonnefil, P., 2008. Age-dependent epigenetic control of differentiation inhibitors is critical for remyelination efficiency. Nat. Neurosci. 11, 1024–1034. https://doi.org/10.1038/nn.2172
Shepherd, G.M.G., 2013. Corticostriatal connectivity and its role in disease. Nat. Rev. Neurosci. 14, 278–291. https://doi.org/10.1038/nrn3469
Shepherd, T.M., Flint, J.J., Thelwall, P.E., Stanisz, G.J., Mareci, T.H., Yachnis, A.T., Blackband, S.J., 2009. Postmortem interval alters the water relaxation and diffusion properties of rat nervous tissue - Implications for MRI studies of human autopsy samples. Neuroimage 44, 820–826. https://doi.org/10.1016/j.neuroimage.2008.09.054
Stafford, J.L., Albert, M.S., Naeser, M.A., Sandor, T., Garvey, A.J., 1988. Age-Related Differences in Computed Tomographic Scan Measurements. Arch. Neurol. 45, 409–415. https://doi.org/10.1001/archneur.1988.00520280055016
Stüber, C., Morawski, M., Schäfer, A., Labadie, C., Wähnert, M., Leuze, C., Streicher, M., Barapatre, N., Reimann, K., Geyer, S., Spemann, D., Turner, R., 2014. Myelin and iron concentration in the human brain: A quantitative study of MRI contrast. Neuroimage 93, 95–106. https://doi.org/10.1016/j.neuroimage.2014.02.026
Tian, Y., Margulies, D.S., Breakspear, M., Zalesky, A., 2020. Topographic organization of the human subcortex unveiled with functional connectivity gradients. Nat. Neurosci. 23, 1421–1432. https://doi.org/10.1038/s41593-020-00711-6
Tovi, M., Ericsson, A., 1992. Measurements of T1 and T2 over time in formalin-fixed human whole-brain specimens. Acta radiol. 33, 400–404. https://doi.org/10.1080/02841859209172021
Trutti, A.C., Fontanesi, L., Mulder, M.J., Bazin, P.-L., Hommel, B., Forstmann, B.U., 2021. A probabilistic atlas of the human ventral tegmental area (VTA) based on 7 Tesla MRI data. Brain Struct. Funct. https://doi.org/10.1007/s00429-021-02231-w
Turner, R., 2019. Myelin and modeling: Bootstrapping cortical microcircuits. Front. Neural Circuits 13, 1–11. https://doi.org/10.3389/fncir.2019.00034
Wagenmakers, E.-J., Farrell, S., 2004. AIC model selection using Akaike weights. Psychon. Bull. Rev. 11, 192–196. https://doi.org/10.3758/BF03206482
Walhovd, K.B., Fjell, A.M., Reinvang, I., Lundervold, A., Dale, A.M., Eilertsen, D.E., Quinn, B.T., Salat, D., Makris, N., Fischl, B., 2005. Effects of age on volumes of cortex, white matter and subcortical structures. Neurobiol. Aging 26, 1261–1270. https://doi.org/10.1016/j.neurobiolaging.2005.05.020
Ward, R.J., Zucca, F.A., Duyn, J.H., Crichton, R.R., Zecca, L., 2014. The role of iron in brain ageing and neurodegenerative disorders. Lancet Neurol. 13, 1045–1060. https://doi.org/10.1016/S1474-4422(14)70117-6
Waskom, M., Seaborn development team, 2020. Seaborn. https://doi.org/10.5281/zenodo.592845
Ye, R., Rua, C., O'Callaghan, C., Jones, P.S., Hezemans, F.H., Kaalund, S.S., Tsvetanov, K.A., Rodgers, C.T., Williams, G., Passamonti, L., Rowe, J.B., 2021. An in vivo probabilistic atlas of the human locus coeruleus at

ultra-high field. Neuroimage 225, 117487. https://doi.org/10.1016/j.neuroimage.2020.117487
Zecca, L., Youdim, M.B.H., Riederer, P., Connor, J.R., Crichton, R.R., 2004. Iron, brain ageing and neurodegenerative disorders. Nat. Rev. Neurosci. 5, 863–873. https://doi.org/10.1038/nrn1537